AIAA JOURNAL
Vol. 32, No. 11, November 1994

Rotor-Rotor Interaction for Counter-Rotating Fans, Part 1: Three-Dimensional Flowfield Measurements

Hyoun-Woo Shin,* Charlotte E. Whitfield,† and David C. Wisler‡
General Electric Aircraft Engines, Cincinnati, Ohio 45215

The rotor wake/vortex flowfield generated in a scale model simulator of General Electric's counter-rotating unducted fan (UDF®) engine was investigated using three-dimensional hot-wire anemometry. The purpose was to obtain a set of benchmark experimental aerodynamic data defining the rotor wake and vortex structure, particularly in the tip region, and to relate this observed flow structure to its acoustic signature. The tests were conducted in a large, freejet anechoic chamber. Measurements of the three components of velocity were made at axial stations upstream and downstream of each rotor for conditions that simulate takeoff, cutback, and approach power. Two different forward blade designs were evaluated. The tip vortices, the axial velocity defect in the vortex core, and differences in the interaction of the wakes and vorticies generated by the forward and aft rotor are used to explain differences in noise generated by the two different rotor designs. Part 1 presents the three-dimensional flowfield measurements. Part 2 (aeroacoustic prediction and analysis), which will be presented later, will give an acoustic prediction using the measured data.

Nomenclature

A = coefficients for curve fit in Eq. (1)
B = blade number
D_1 = distance between forward blade tip to tip
M_∞ = freestream Mach number
R, R_1 = radius to tip of forward blade
r = radial distance
T = time period for one revolution
t = time
U = absolute velocity
U_e = effective velocity
U_t = tangential velocity
U_x = axial velocity
U_∞ = freestream velocity
V^+ = periodic unsteady transverse velocity
x = axial distance
α = angle between probe sensor and flow direction
θ_p = pitch angle
θ_y = yaw angle
θ_0 = sensor angle

I. Introduction and Objectives

DURING the 1980s, the concept of a counter-rotating unducted fan engine attracted considerable attention from the aircraft industry because of its higher propulsion efficiency and lower specific fuel consumption relative to current high bypass turbofan engines of equivalent thrust.[1,2] A primary concern in the development of this engine concept was that the cabin interior noise levels and the far-field community noise levels should be comparable to or lower than current high-bypass turbofan noise levels.

Consequently, an extensive scale-model test program was undertaken to investigate the influence of various geometric and aerodynamic parameters on the performance and noise characteristics of swept, counter-rotating propellers.[3]

Propeller system design has a direct impact on aircraft performance and efficiency, and that impact is greatly dependent on the flowfield around the propellers. Because of the difficulty in making detailed and accurate measurements, very little was known about these flowfields until 1985 when NASA initiated a broad research program which attempted to acquire basic aerodynamic data on the installation effects of advanced turboprop concepts. A number of test programs were initiated. Detailed flowfield measurements around single-rotating propeller and counter-rotating propeller nacelle configurations[4] were made using laser velocimetry. These measurements illustrate the application of the laser velocimetry technique as a diagnostic tool and provide preliminary averaged data. Podboy and Krupar[5] measured the wakes both between and downstream of the rotors of a counter-rotating unducted fan model operating at cruise conditions. Their experiment employed the use of a four-beam two-color laser Doppler velocimetry system

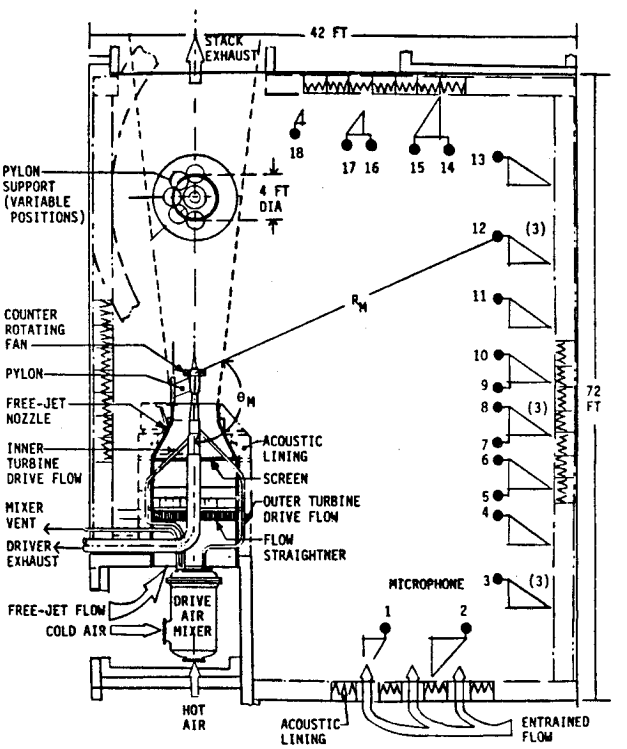

Fig. 1 Model simulator installation and anechoic chamber.

Presented as Paper 93-1848 at the AIAA/SAE/ASME/ASEE 29th Joint Propulsion Conference, Monterey, CA, June 28–30, 1993; received Aug. 20, 1993; revision received March 14, 1994; accepted for publication April 18, 1994.

*Staff Engineer, Aerodynamics Research Laboratory.
†Engineer, HSCT Acoustics & Nozzle Performance Integration. Member AIAA.
‡Manager, Aerodynamics Research Laboratory. Member AIAA.

which could be synchronized to either rotor. Because of the two-dimensional system, they had to obtain the third component of velocity later. The data measured downstream of the front rotor characterize the tip vortices, vortex sheets, and potential field nonuniformities generated by the front rotor with limited data points between rotor blades. Tillman et al.[6] used a single- and a multisensor hot-wire measurement technique to acquire blade-synchronized, three-dimensional periodic velocity downstream of a single rotation prop fan operating at a simulated cruise condition. The technique also required the third component of velocity to be obtained later.

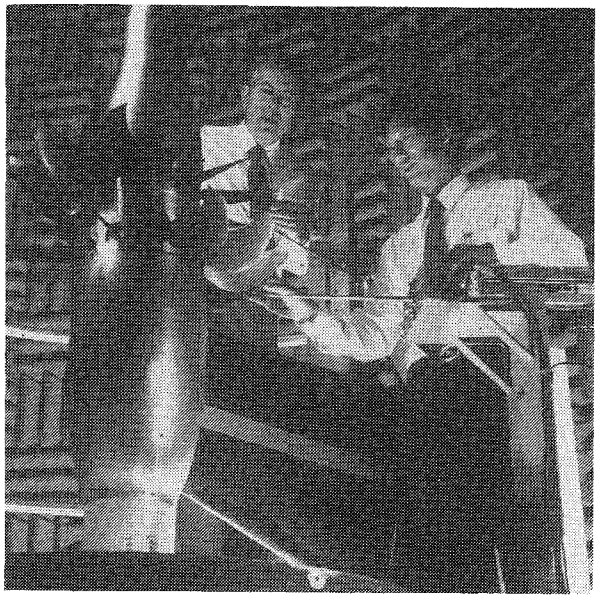

Fig. 2 Photograph of the MPS.

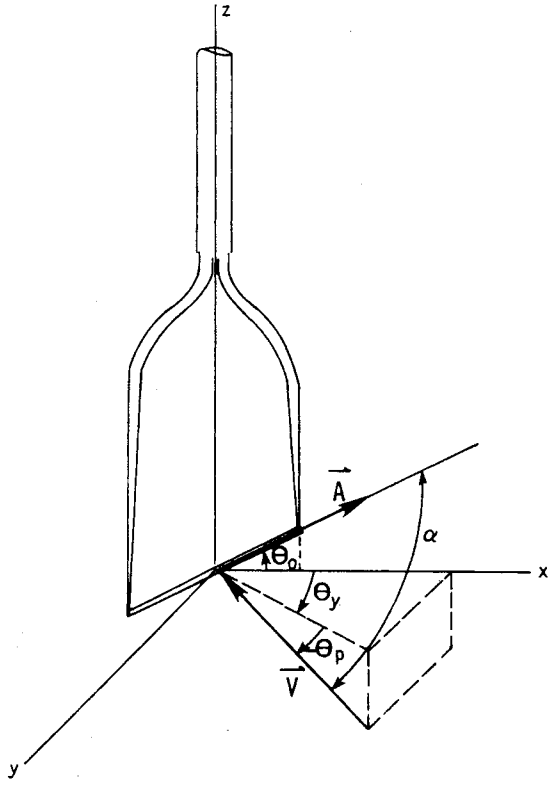

Fig. 3 Hot-wire configuration relating velocity vector v to hot-wire sensor and probe coordinates x, y, and z.

For this study, a single, slanted hot wire was used to obtain three-dimensional velocity information for the flowfield generated by a scale-model unducted fan (UDF®) engine. The computer-controlled anemometer system took three-dimensional velocities at locations upstream, downstream, and between the rotors. For the first time the location of the tip vortex from the forward blade row was tracked to its impingement point on the aft blade row using the hot-wire measurement technique. In addition, this vortex was also located downstream of the aft blade row.

The objectives of this project were to obtain a set of benchmark experimental aerodynamic data defining the rotor wake and vortex structure, particularly in the tip region, and to relate this observed flow structure to its acoustic signature.

II. Description of Experiment

A. Anechoic Freejet Facility

The anechoic facility, shown schematically in Fig. 1, is a cylindrical chamber 45 ft in diameter and 72 ft in height. The air supply for flight simulation is obtained from a freejet air system consisting of a large fan driven by an electric motor. The air from this fan is routed through a transition duct, a silencer plenum chamber, and screens. It is then discharged through a 4-ft-diam exhaust nozzle to become the freestream air approaching the counter-rotating blading of the flight simulator. The freejet Mach number can be varied by controlling the air flow rate with adjustable fan inlet vanes to permit Mach numbers up to 0.3 at the nozzle exit. The model propulsion simulator (MPS) is attached to the freejet nozzle using three support struts. The centerline of the simulator coincides with the centerline of the freejet nozzle. The air for the turbine, which is used to drive the counter-rotating propulsor blades, is supplied at the base of the support stand. Acoustic signatures were obtained from the 18 microphones located at the positions shown in Fig. 1. A photograph of the MPS is shown in Fig. 2.

B. Measurement Technique

A single, 45-deg slanted hot-film sensor, TSI Model 1213-20, was used with a TSI IFA 100-4 anemometer to measure three-dimensional velocities. Data were passed through a KineticSystem analog-to-digital (A/D) converter with memory modules into a microVAX II computer.

The hot-film probes were calibrated in the potential core of a precision calibration jet over a velocity range from 0 to 700 ft/s and over the expected yaw and pitch angles of the MPS flowfield. The output is correlated to the fluid velocity with a fourth-order fit, showing that the anemometer signal could be linearized by the software.

The effective cooling-velocity calibration was performed to obtain the coefficients of the effective cooling-velocity ratio in Eq. (1). Previous experiments conducted by Shin et al.[7] and Shin and Hu[8] showed that this velocity ratio was strongly dependent on the sensor yaw angle and weakly dependent on the pitch angle and velocity level. The recommended correlation is as follows:

$$U_e/U = A_0 + A_1\alpha + A_2\theta_p + A_3U + A_4\alpha\theta_p + A_5\alpha V + A_6\theta_p V + A_7\theta_p^2 + A_8\alpha^2 + A_9\alpha^3 \quad (1)$$

where $\cos\alpha = \cos\theta_0 \cos\theta_p \cos\theta_y - \sin\theta_0 \sin\theta_p$.

The hot-wire sensor, the probe coordinate system, and a general velocity vector are shown in Fig. 3. For a particular velocity level, the probe was set at each of five pitch angles and rotated from −90 to 90 deg in yaw angle increments of 10 deg. This procedure was continued until data at two velocity levels and pitch angles (−20 deg to 20 deg, increments of 10 deg) were acquired. After all of the data were taken, the coefficients were obtained using a least squares method.

The error on the magnitude of absolute velocity is about 2.0% of a measured velocity, and the error on both yaw and pitch angles is about 0.75 deg including a probe installation and a least square curve fit errors.

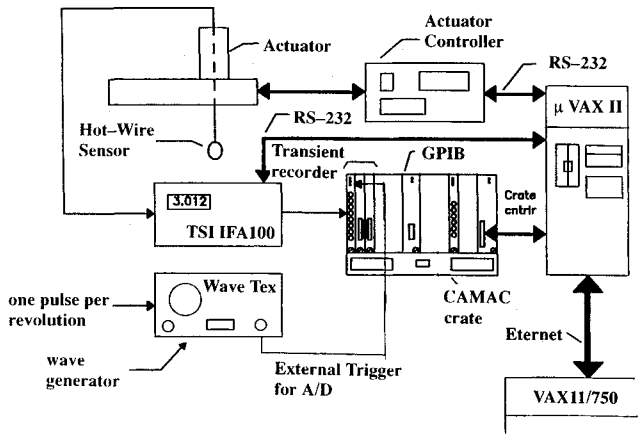

Fig. 4a Hot-wire data acquisition.

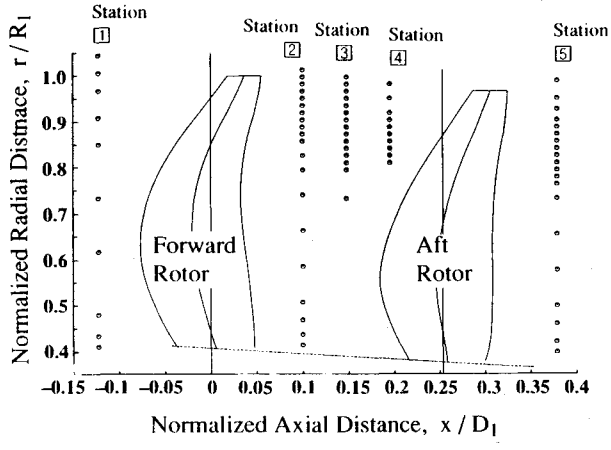

Fig. 4b Axial projection of propeller model showing hot-wire measurement location as small circles.

C. Blading

The scale-model MPS configuration has a blade tip diameter of 25.7 in. with a 0.40 hub-to-tip radius ratio. There are 12 forward rotor blades and 10 aft rotor blades. The counter-rotating blades were spaced approximately 7 in. apart for optimum acoustics. The unducted fan blade configuration A was designed in a scale model to maximize the fan efficiency at the Mach 0.78, 35,000-ft altitude condition. The airfoils of configuration A were designed to be efficient at high relative Mach numbers and moderate lift coefficients. Configuration B was designed for low community noise at a Mach 0.25, sea level takeoff condition. The 12+10 counter-rotating blade airfoils were shaped specifically to produce good aerodynamic performance at the takeoff condition, thereby reducing the noise signature through lower aerodynamic losses. In contrast to configuration A, configuration B airfoils were designed to be efficient at high lift coefficients and moderate relative Mach numbers. Other geometric parameters were similar to configuration A.

D. Test Procedure

The MPS tunnel conditions (setpoints) were established by obtaining equal torque on the front and aft rotors. During the course of this study, three thrust levels were used. They were 630, 444, and 220 lb equivalent to takeoff, cutback, and approach conditions. Two hot-wire probes were used to measure velocity from the upstream of the front rotor, the region between front and aft rotors and the downstream of aft rotor.

E. Data Acquisition and Data Reduction

The data acquisition process for sampling the hot-film output voltages is shown in Fig. 4a and discussed briefly subsequently. The raw signal from the bridge output contained random as well as phase related information. The data were ensemble averaged to remove the random component. With the probe sensor positioned at 90 deg (normal to the MPS axis), the probe was rotated to the three different yaw angles at which data were acquired. A rotor 1/rev signal was fed into the external trigger input of a WaveTech Model 145 signal generator to generate a sharp −5 V pulse which was fed into the stop trigger of the A/D converter module. The A/D converter speed was set to 100 kHz and a 2000 sample memory was allocated in the 2 megasample memory module operating in a post trigger mode. The data acquisition program initialized the A/D converter and located the probe for the first measurement position. The hot-film signals were digitized but were not stored in memory until the A/D converter received the trigger signal from the signal generator. Data were taken for 2.5 ms, about 2.5 blade passages, at each probe angle position and transported to the computer. The instantaneous voltage data were converted to the effective velocity level using the velocity calibration information. At each of 250 phase-locked positions 300 sets of data were taken and averaged. Figure 4b shows the survey lines and the radial locations where data points were obtained. The data were transported, reduced, and analyzed using a Digital Equipment VAX 11/750 computer. The data were reduced by solving six nonlinear equations simultaneously using the hybrid method[11] to obtain velocity, yaw (circumferential direction), and pitch (radial direction) angles.

III. Results and Discussion

Hot-wire measurements were taken with six different blade designs. In this paper only two forward rotor blade designs, A and B described earlier, will be discussed.

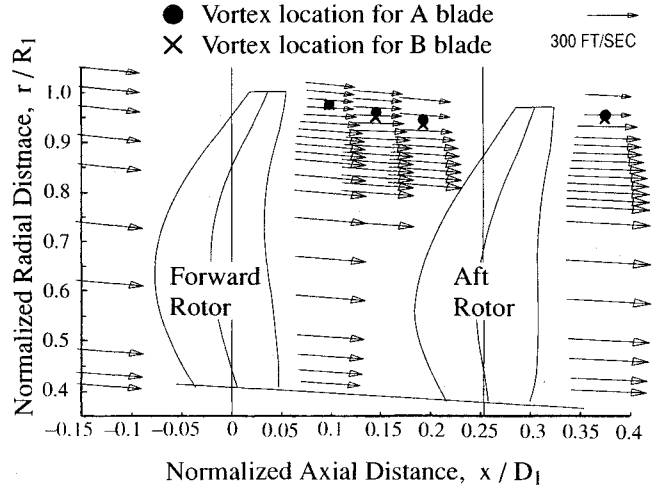

a) Takeoff setting, blade A, freejet M_∞ = 0.25

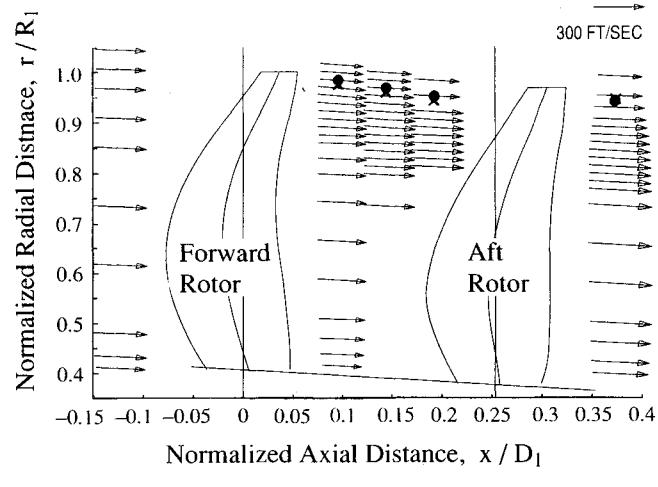

b) Approach setting, blade A, freejet M_∞ = 0.20

Fig. 5 Circumferential-averaged axial velocity showing tracking of tip vortex.

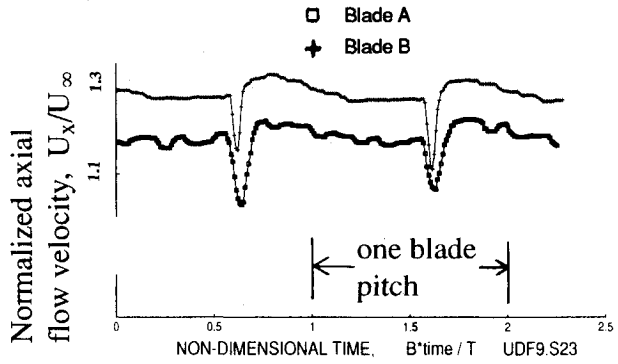

a) $r/R = 0.888$

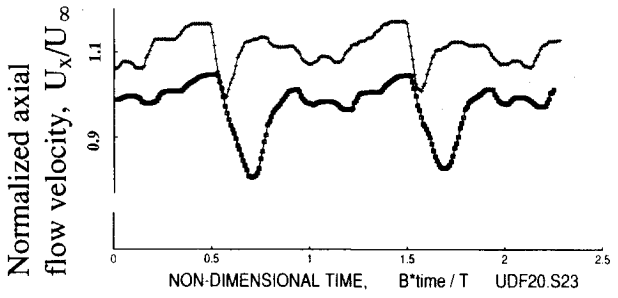

b) $r/R = 0.413$

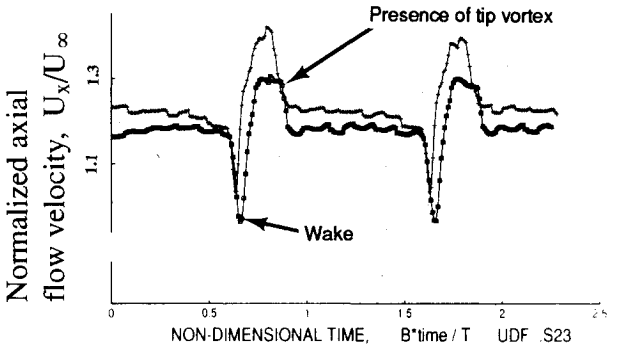

c) $r/R = 0.951$

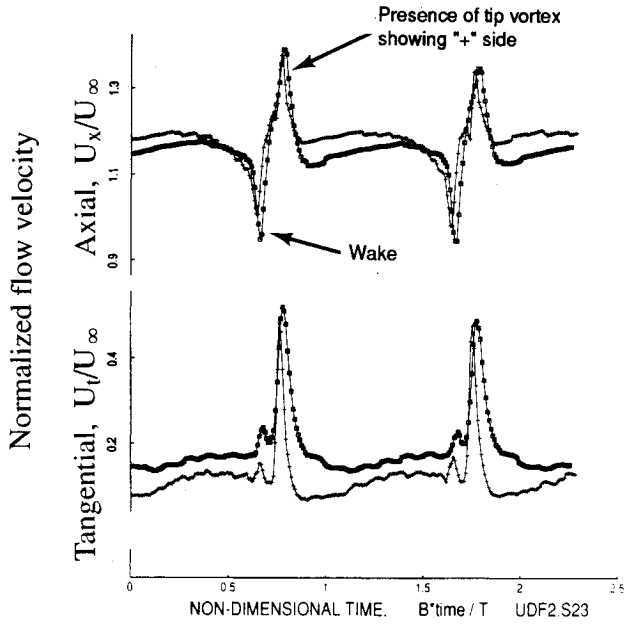

d) $r/R = 0.967$

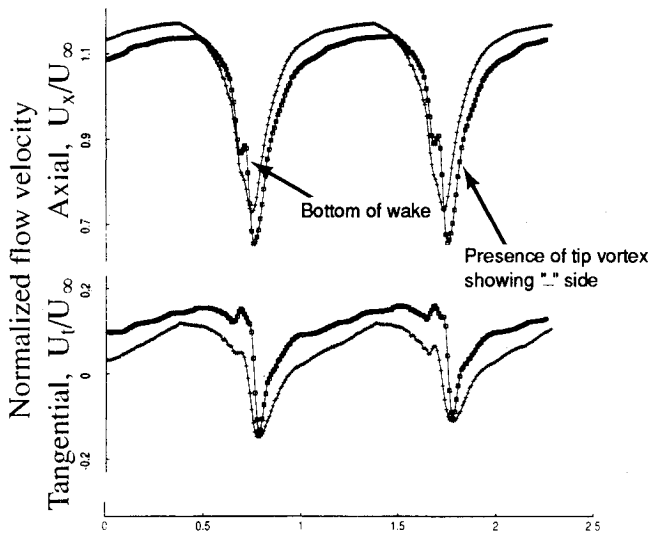

e) $r/R = 0.982$

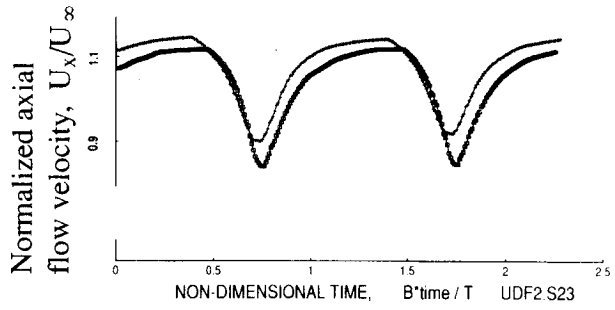

f) $r/R = 0.998$

Fig. 6 Phase-locked averaged velocities at station 2 with blade A, approach condition.

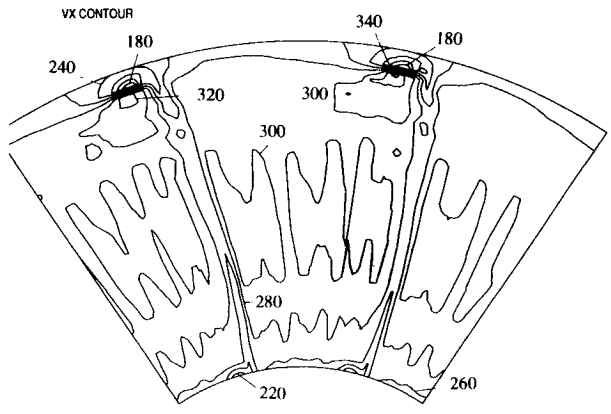

Fig. 7 Axial velocity contour plot at station 2 with blade A, approach condition.

The flowfields were measured at numerous radial locations and at three axial stations between the forward and aft rotors and one axial station each upstream of the forward rotor and downstream of the aft rotor as shown in Fig. 4b. The flowfield measurements between the two rotors give a better understanding of the flowfield disturbances present in the wake of the advanced propeller. The flowfield disturbances of interest are the tip vortex and the viscous blade wakes, because noise is generated when these nonuniformities interact with the downstream rotor blades. The tip vortices and the blade wakes are generally considered to be the major contributors to this interaction noise.[12]

A. Circumferentially Averaged Velocity Vectors

The circumferentially averaged velocity vectors at the five different axial locations are shown in Figs. 5a and 5b for two different

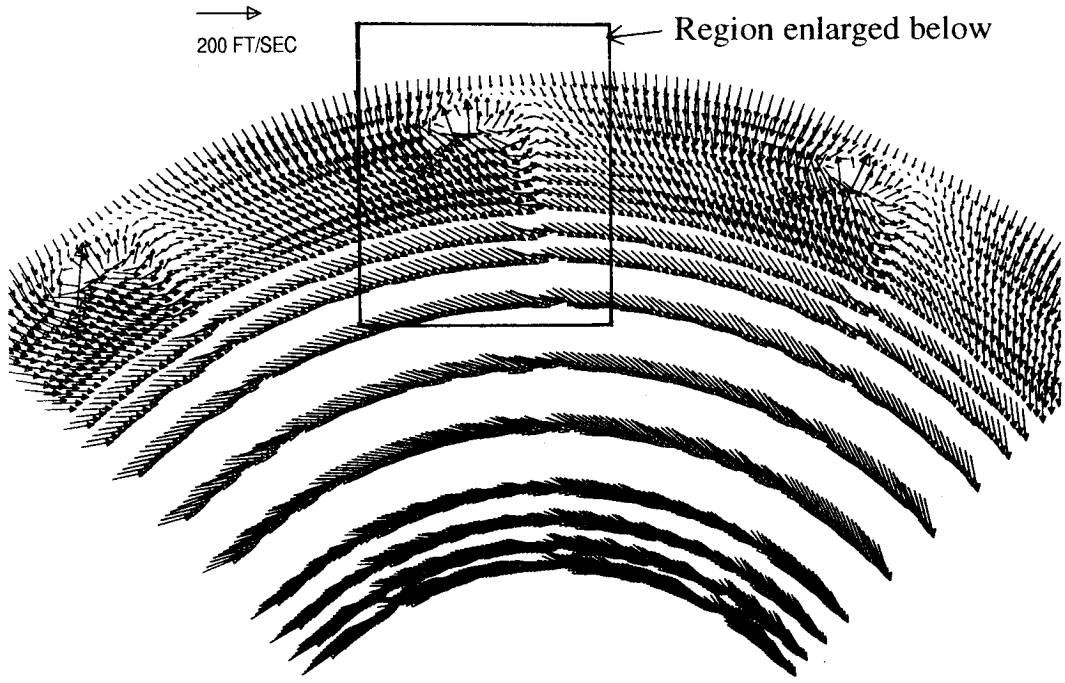

a) Blade B, M_∞=0.25, cutback at station 2

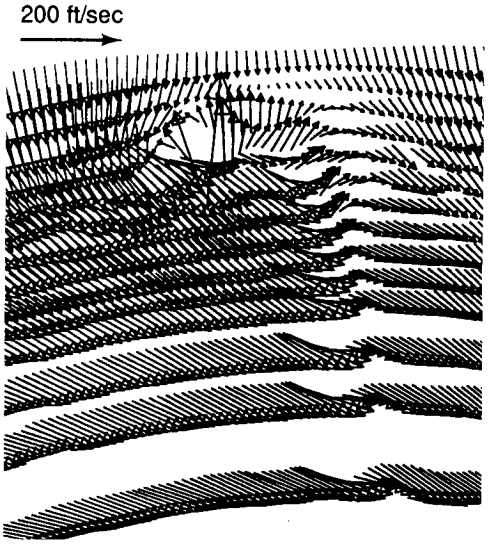

b) Enlarged region from part a

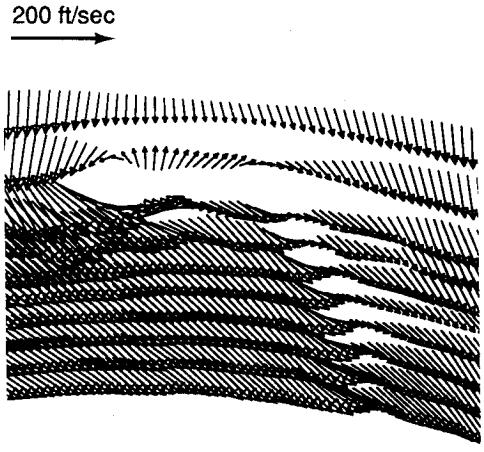

d) Blade B, M_∞ = 0.22, cutback at station 4

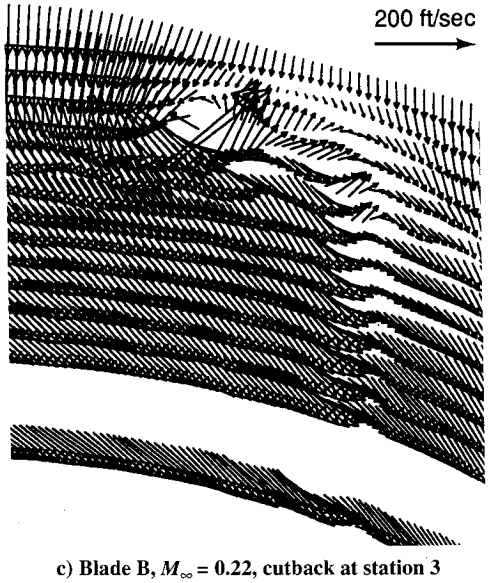

c) Blade B, M_∞ = 0.22, cutback at station 3

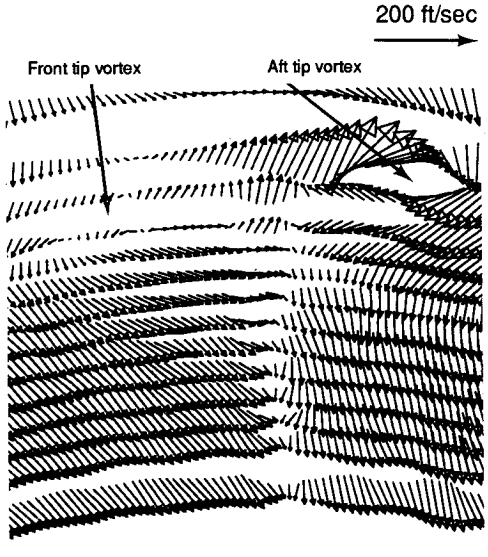

e) Blade B, M_∞ = 0.22, cutback at station 5

Fig. 8 Phase-locked averaged velocities measured in r-θ plane at axial stations 2–5, blade B, M_∞ = 0.25, cutback setting.

power levels for blading A. The figure shows not only the track of the vortices shed from the forward rotor but also the radially inward movement of the flow downstream of the front rotor. This inward flow is redirected close to the axial direction downstream of the aft rotor. Figure 5 indicates that the tip vortex from blading B moves only very slightly farther inward than that for blading A.

B. Velocity Distributions Downstream of the Front Rotor

Typical hot-wire measurements are presented in Fig. 6. This figure shows plots of axial and tangential velocity components, normalized by the freejet velocity, as a function of the parameter Bt/T, where $Bt/T = 1$ corresponds to one blade passage. The sign convention is such that positive axial velocity is in the downstream direction, positive tangential velocity is the same as the direction of forward blade rotation, and positive radial velocity is outward from the hub. The data shown in Fig. 6 were acquired at 2.5-ms intervals, giving 250 data points over 2.25 blade passages at approach conditions at station 2 in Fig. 4. The viscous wakes, near midspan and near the hub shown for $r/R = 0.888$ and 0.413 in Figs. 6a and 6b, respectively, are classically asymmetric. The wake profile has spread out and is deeper in magnitude near the hub due to interaction with the hub boundary layer. As one moves radially outward to $r/R = 0.951$, the effects of the tip vortex/leading-edge vortex become evident in the data shown in Figs. 6c and 6d. In this region, a hump appears in the axial velocity distribution just after the viscous wake as marked in the figure. The presence of this axial velocity peak is due in part to the manner in which the blade tip vortex/leading-edge vortex convects downstream after leaving the blade. That vortex swirl velocity has a component which adds positively to the axial velocity on the inboard side of the vortex. A drastic change can be found in the character of the axial velocity at $r/R = 0.982$ as shown in Fig. 6e. There is a large axial velocity defect associated with the outboard portion of the vortex because the swirl on the outboard side of the vortex has a component which adds negatively to the axial velocity. The bottom of the wake was captured, as marked in the figure, indicating that the velocity defect still contained the rotor wake at that location. The velocity defect is wider and about half the magnitude at $r/R = 0.998$ where a rotor wake no longer exists as shown in Fig. 6f. These results are summarized in the contour plot of axial velocity shown in Fig. 7. The velocity defect in the core of the tip vortex and in the blade wake are clearly evident.

The tangential velocities have unique features attributed to the presence of the vortex structure. These are shown in Figs. 6d and 6e. At $r/R = 0.982$, a negative pulse of tangential velocity is generated as the blade passes, indicating vortex swirl in the opposite direction to the rotation. As one moves inward, the tangential velocity profiles become narrow and pronounced in magnitude, much like the axial velocity. At $r/R = 0.967$ the tangential velocity shows evidence that the inboard portion of the vortex has been reached. In addition, one notices a difference between blades A and B. Blade B has a narrower vortex structure than blade A indicating less vortex disturbance.

C. Phase-Locked Averaged Velocities in Propeller Plane of Rotation

The phase-locked averaged velocities measured at axial stations 2–5 of Fig. 4 are presented in Figs. 8b–8e, respectively. The secondary velocity vectors clearly show the turning of the flow produced by the rotating blades. The data of Fig. 8 also indicate the presence of a tip vortex and a wake from the blade. The continued rollup of the vortex can be observed by sequential reference to Figs. 8 from part 8b–8d. The secondary velocity vectors plotted in these figures suggest that the tip vortex gets larger with increased distance downstream of the front rotor. The rotational velocities are much larger on the suction side of the vortex. The increase in the velocities on this side of the core may be attributed to the overall inward movement of the flow that results from the narrowing contour of the contraction of the stream tube. On the pressure side of the vortex this radial inflow is in a direction opposite to the flow produced by the vortex. Conversely, on the suction side of the vortex, the inflow and the vortex flow are in the same direction. The superposition of these two flows results in larger secondary velocities in the suction side of the core. Moving behind the aft rotor gives a tip vortex of opposite direction as seen in Fig. 8e where most of the swirling flow has been eliminated downstream of the aft rotor. The rotor wake areas are identified from these figures. The spanwise extent and core location of the aft and forward rotor tip vortices can be estimated from Fig. 8. The tip vortex comparison between three different power levels is shown in Fig. 9. The figure shows clear indication of the different size of the tip vortex generated by the front rotor. The high power level generated a strong small core size of tip vortex.

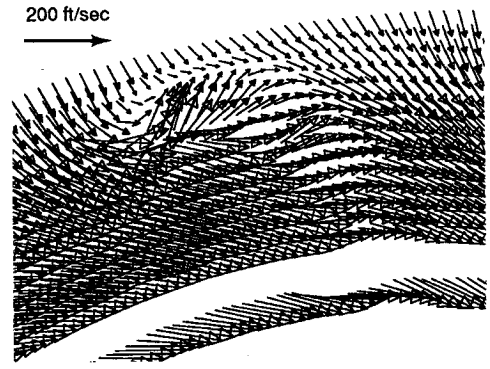

a) Blade A, $M_\infty = 0.25$, takeoff at station 3

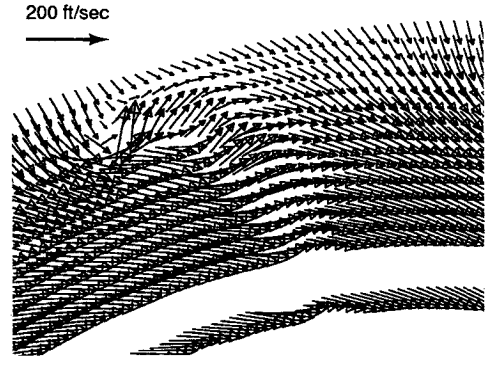

b) Blade A, $M_\infty = 0.25$, cutback at station 3

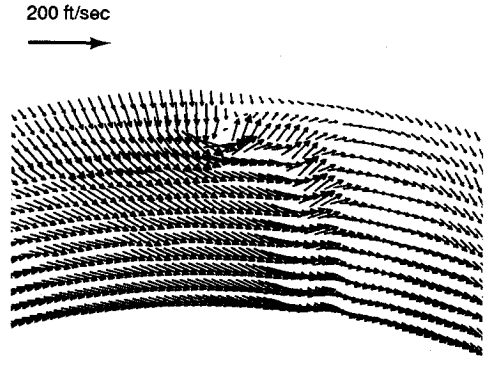

c) Blade A, $M_\infty = 0.20$, approach at station 3

Fig. 9 Phase-locked averaged velocities measured at station 3 with various thrust levels.

D. Contour Plots of Vorticity

Contours of the axial vorticity calculated using the secondary velocity vectors downstream of the forward and aft rotors are shown in Fig. 10. These contours provide a good indication of the spatial extent of the relatively small region within the passage that contains the axial vorticity shed from a forward and an aft rotor blade. The amount of noise generated by a tip vortex as it interacts with a downstream rotor blade is dependent on the strength of the vortex and the extent to which the vortex is intercepted by the blade. This series of contour plots also shows the blade wake vor-

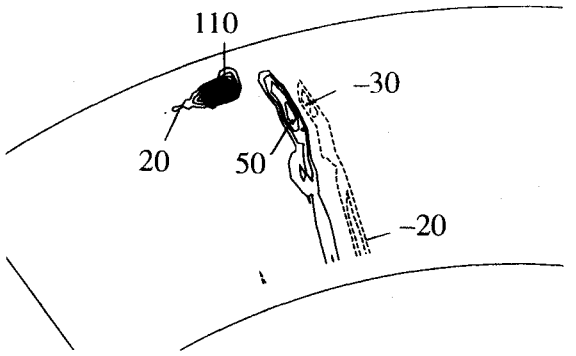

a) Blade A, approach at station 2

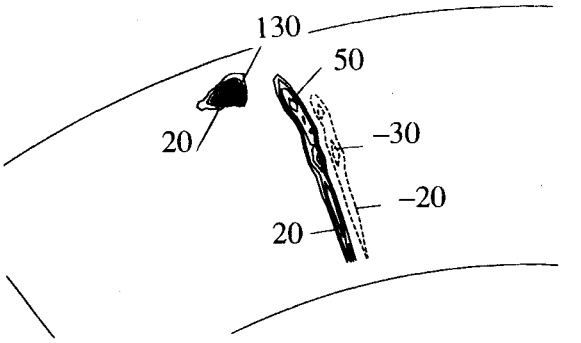

e) Blade B, approach at station 2

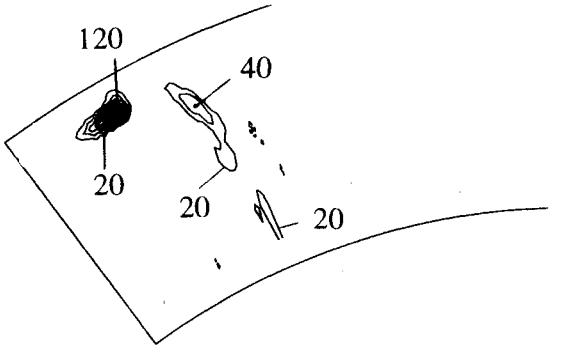

b) Blade A, approach at station 3

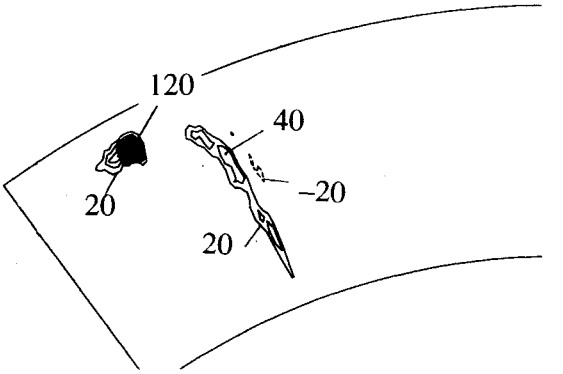

f) Blade B, approach at station 3

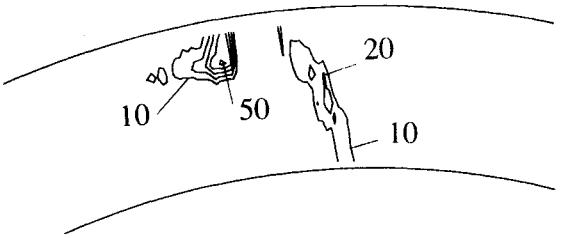

c) Blade A, approach at station 4

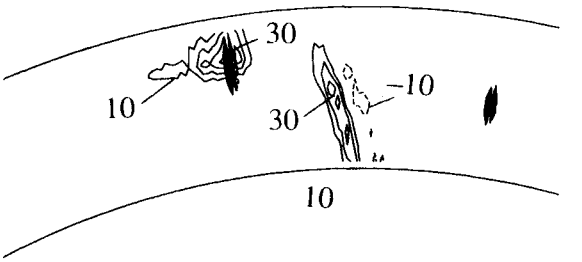

g) Blade B, approach at station 4

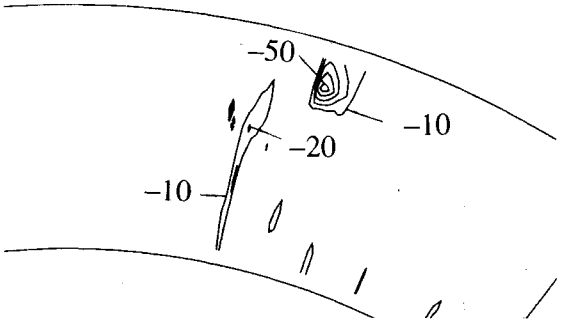

d) Blade A, approach at station 5

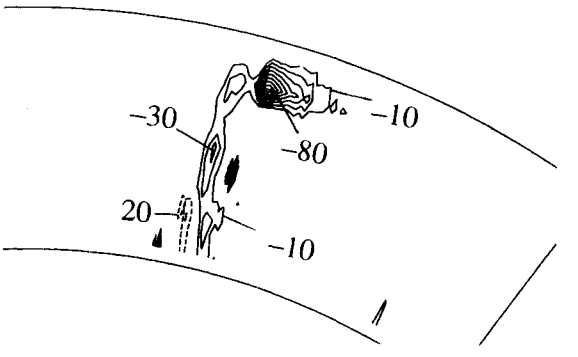

h) Blade B, approach at station 5

Fig. 10 Vorticity contour plots, $M = 0.22$.

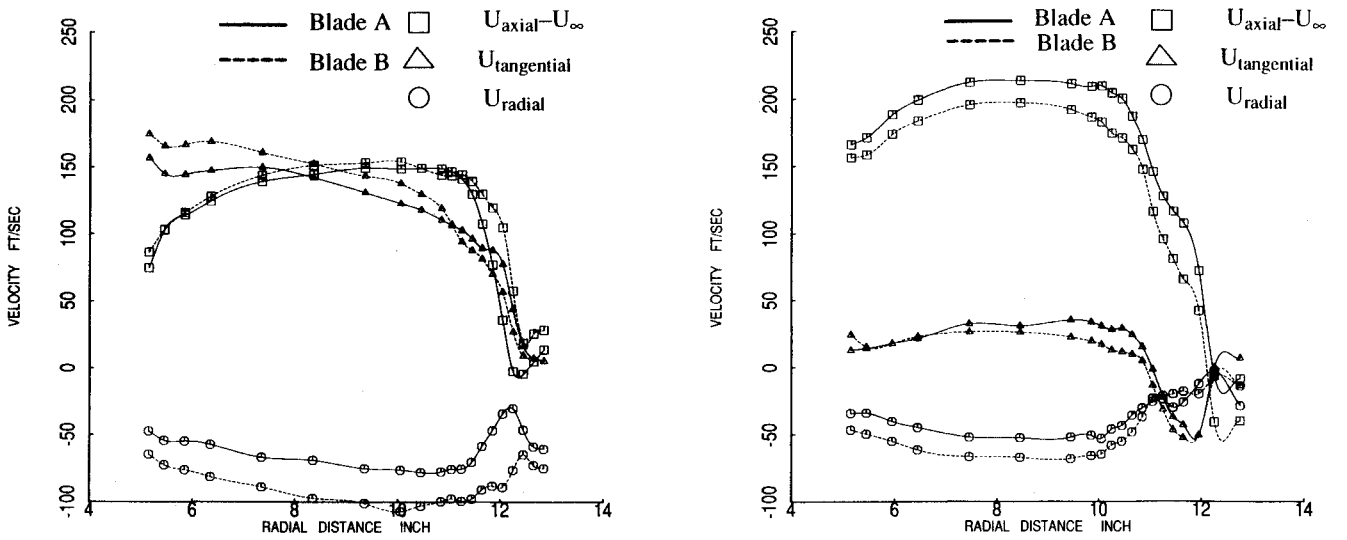

Fig. 11 Spanwise distribution of circumferential averaged axial, tangential, and radial velocities.

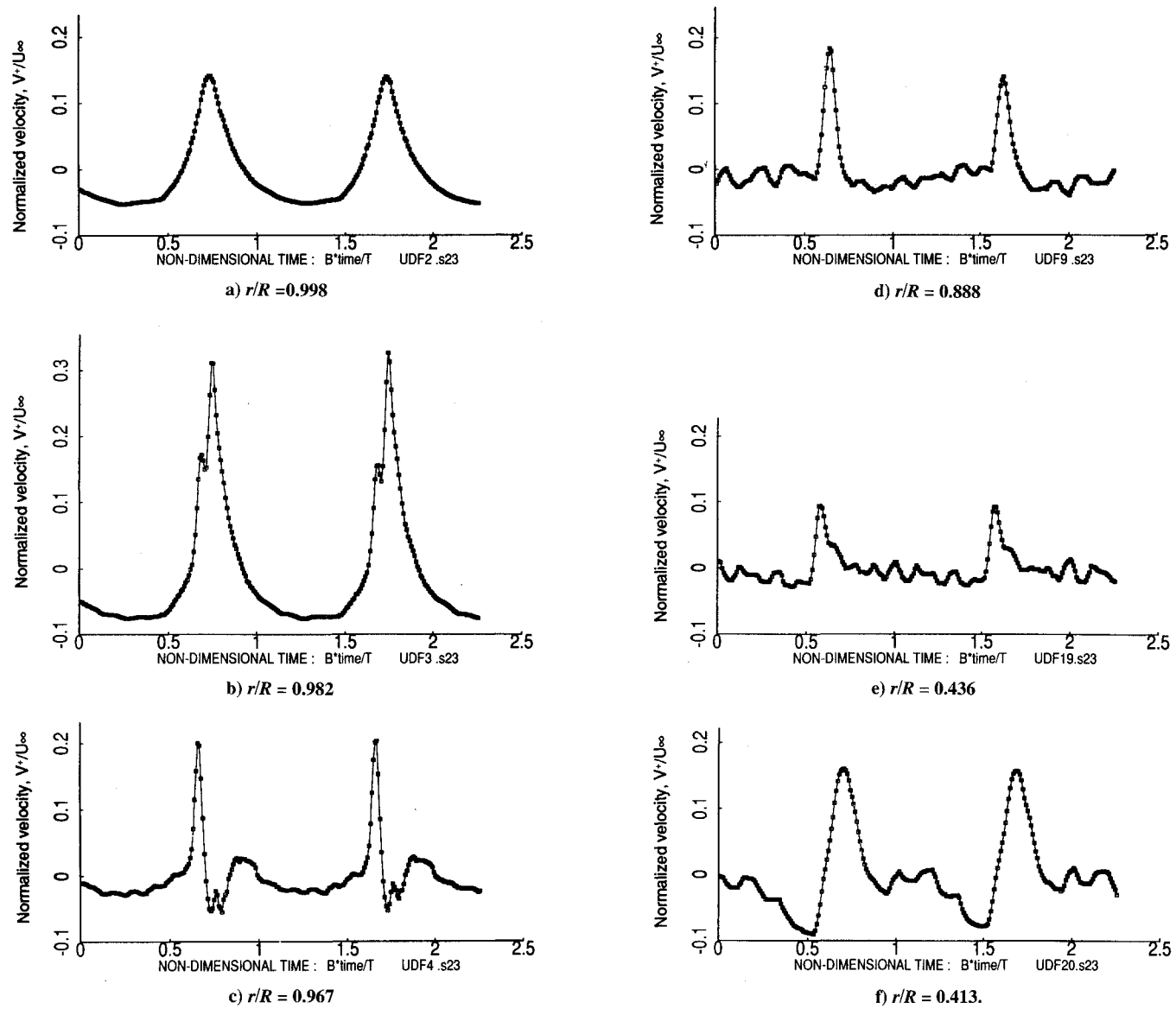

a) r/R =0.998

d) r/R = 0.888

b) r/R = 0.982

e) r/R = 0.436

c) r/R = 0.967

f) r/R = 0.413.

Fig. 12 Distribution of V^+ at station 2 with blade A, approach condition.

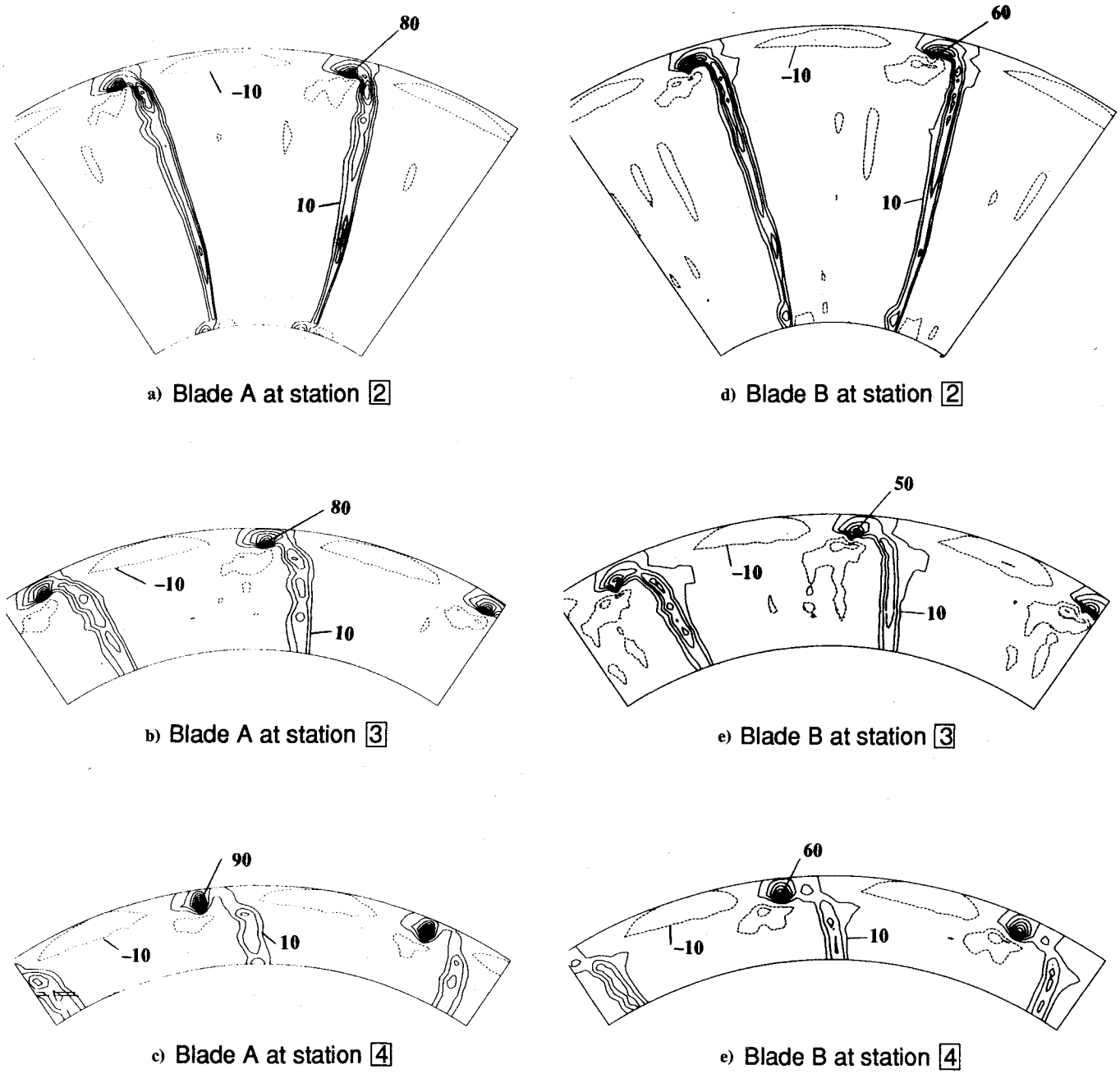

Fig. 13 Contour comparison of V^+ between blade A and B at axial stations 2–4, contour interval 10.

tex sheet being deformed and weakened as it is convected downstream. The plots also suggest that as the vortices move downstream, the tip vortex and the wake vortex sheet may actually be separating. Blade B generated a slightly stronger tip vortex than blade A at station 2.

E. Spanwise Distributions of the Circumferentially Averaged Velocities

The spanwise distributions of the circumferentially averaged axial, tangential, and radial velocities measured at axial stations 2 and 5 at the takeoff condition are shown in Fig. 11. The axial velocity distributions are plotted minus the freestream velocity. The thrust contribution supplied by the aft rotor is evidenced by the increase in axial velocity that is shown to occur between these two stations. Blade A produced higher thrust than blade B. The radial velocity distribution indicates a rather large jump in magnitude across the span of the aft rotor. These radial velocities become less negative at station 5, downstream of aft the rotor, thereby indicating that the radial flow angle was redirected close to the axial direction. The tangential velocity distribution along the radial direction measured downstream of the aft rotor shows that the aft rotor blades eliminate most of the swirl flow generated by the front rotor. This is the major advantage of counter-rotating propeller over single rotating ones. This allows the second rotor to redirect the swirling flow exiting the front rotor back into the axial direction.

F. Periodic Unsteady Transverse Velocities

The figures presented thus far have shown the forward-rotor-synchronized flowfield as perceived by a stationary observer. The main source of noise from counter-rotating open rotors under takeoff conditions results from fluctuating aerodynamic loading in the aft rotor caused by the periodic wake/vortex flowfield generated by the forward rotor. Estimation of this rotor-rotor interaction noise[12] requires the evaluation of the flowfield in the rotating frame of reference of the aft rotor, in particular, that component normal to the relative velocity at the blade leading edge. The periodic unsteady transverse velocities V^+ were computed by constructing instantaneous vector diagrams, with the ensemble-averaged velocities and

the instantaneous velocities as follows. The time-mean velocity was determined by arithmetically averaging the ensemble-averaged velocities for all of the equally spaced time increments across the blade spacings. From this, a single time-mean vector diagram was constructed. Then for each of the time increments, an instantaneous vector diagram was computed. From the one steady and the many instantaneous vector diagrams, the periodic unsteady velocities V^+ were computed.[13] Figures 12 and 13 show this V^+ component of velocity. The strong effect of the tip vortex can be seen clearly in the tip region, with an increase also toward the hub. Acoustically, it is the tip region that is of the most concern as the faster moving sources (in this case, the blades) radiate sound more efficiently. Figure 13 shows clearly that, in contrast to the impression left by examination of the flowfield in the stationary reference frame, blade B should generate less rotor-rotor interaction noise than blade A. Acoustic analysis will be presented in Part II of this paper.

IV. Conclusions

Data have been presented to define the three-dimensional flowfield generated by counter-rotating blades. In addition, the hot-wire measurement technique using a slanted hot-wire probe has been successfully developed and adopted to acquire the present set of data from a scale model UDF® engine. The following observations can be made from the data presented herein.

1) An axial velocity defect in a vortex core was identified in the outboard portion of the tip vortex. The magnitude of the defect was larger than that seen in the blade wake region.

2) The tip vortices shed from the forward rotor blades grew in size but diminished in strength as they were convected downstream. The forward rotor vortex was identified downstream of the aft rotor.

3) The impact location of the vortex shed from the forward rotor with the aft rotor could be located by finding the trace of the forward rotor vortex.

4) The radial distribution of three components of velocity obtained upstream and downstream of the aft rotor showed the aft rotor contributed thrust and eliminated most of the swirl generated by the front rotor.

5) The measured component of fluctuating velocity normal to the relative velocity entering the aft rotor indicates that different noise levels would be obtained from the two forward rotor blade designs tested here.

Acknowledgments

The authors are deeply indebted to the following people for their support during the testing: Philip R. Gliebe, manager of Acoustic Systems Technology for support of the program; Gregory Hoff, senior engineer in Installed Performance Test/Analysis and Test Cell 41 crew; and Joseph Hencheck, Michael Carroll, and William Niehoff for running the test rig. The authors also wish to thank General Electric Aircraft Engines for permission to publish this paper.

References

[1]Brahney, J. H., "Is the Unducted Fan Tomorrow's Subsonic Engine?," *Aerospace Engineering*, Vol. 5, No. 2, 1985, pp. 7–10.

[2]Smith, L. H., Jr., "Unducted Fan Aerodynamic Design," *Journal of Turbomachinary*, Vol. 109, No. 3, 1987, pp. 313–324.

[3]Janardan, B. A., Chuang, S., Ho, P. Y., and Lee, R., "Scale Model Acoustic Testing of Counter-rotating Fans," AIAA Paper 88-2057, May 1988.

[4]Dunham, D. M., and Sellers, W. L., III, "Laser Velocimeter Measurements of the Flow Fields around Single and Counter-Rotating Propeller Models," Society of Automotive Engineers, Tech. Paper 850870, April 1985.

[5]Podboy, G. G., and Krupar, M. J., "Laser Velocimeter Measurements of the Flow Fields Generated by an Advanced Counter-rotating Propeller," NASA TM 101437, 1989; also AIAA Paper 89-0434, Jan. 1989.

[6]Tillman, T. G., Simonich, J. C., and Wagner, J. H., "Hot Wire Measurements Downstream of a Prop-Fan," AIAA Paper 89-2698, July 1989.

[7]Shin, H.-W., Cheng, W. K., Greitzer, E. M., and Tan, C. S., "Inlet Vortex Formation Due To Ambient Vorticity Intensification," *AIAA Journal*, Vol. 24, No. 4, 1986, pp. 687–689.

[8]Shin, H.-W., and Hu, Z., "Measurement of Swirling Flow Field Using the Single Slanted Hot Wire Technique," *International Journal of Turbo and Jet Engines*,Vol. 3, No. 2–3, 1986, pp.139–145.

[9]Miller, C., and Podboy, G. G., "Euler Analysis with LDA Data for an Advanced Counter-Rotation Propfan at Cruise," AIAA Paper 90-3033 Aug. 1990.

[10]Wagner, J. H., and Okiishi, T. H., "Analysis of Multistage, Axial Flow Turbomachine Wake Production, Transport, and Interaction," Engineering Research Inst., Iowa State Univ., ISU-ERI-AMES-78173, TCRL-10 ERI Project 1204, Dec. 1977.

[11]Powell, M. J. D., "A Hybrid Method for Nonlinear Equations," Mathematics Branch, Theoretical Physics Div., Atomic Energy Research Establishment, Harwell, Berkshire, England, UK; also *Numerical Methods for Nonlinear Algebra Equations*, edited by P. Rabinozitz, Gordon & Breach, London, 1970, Chap. 6.

[12]Whitfield, C. E., and Gliebe, P. R., "Predicted vs. Scale Model and Flight Test UDF® Engine Noise," AIAA Paper 90-3936, Oct. 1990.

[13]Manwaring, S. R., and Wisler, D. C., "Unsteady Aerodynamics and Gust Response in Compressors and Turbines," American Society of Mechanical Engineers, ASME 92-GT-422, June 1992.